OPTICS

Metaform optics: Bridging nanophotonics and freeform optics

Daniel K. Nikolov[1], Aaron Bauer[1], Fei Cheng[1], Hitoshi Kato[2], A. Nick Vamivakas[1,3,4,5]*, Jannick P. Rolland[1,6,7]*

The demand for high-resolution optical systems with a compact form factor, such as augmented reality displays, sensors, and mobile cameras, requires creating new optical component architectures. Advances in the design and fabrication of freeform optics and metasurfaces make them potential solutions to address the previous needs. Here, we introduce the concept of a metaform—an optical surface that integrates the combined benefits of a freeform optic and a metasurface into a single optical component. We experimentally realized a miniature imager using a metaform mirror. The mirror is fabricated via an enhanced electron beam lithography process on a freeform substrate. The design degrees of freedom enabled by a metaform will support a new generation of optical systems.

INTRODUCTION

Locally and globally customizable optical response of devices with minimal form factor is the "holy grail" for the optical design of novel imaging systems such as augmented and virtual reality (AR/VR) displays, three-dimensional (3D) depth vision, mobile cameras, remote sensing, and more (*1*–*17*). Recent advances in the design, fabrication, and testing of metasurfaces and freeform optics have made these two technologies well fit to address the needs of this emerging generation of optical systems (*18*, *19*). To understand the impact of these optical devices on optical design, let us consider the basic function of imaging systems.

The propagation of light through an optical system can be studied by describing light as rays or waves. These two perspectives are interchangeable in the geometric optics approximation regime, where the optical surface features are on a scale much larger than the wavelength of light (*20*). The wavefronts, defined as equiphase fronts, are surfaces perpendicular to the rays in a homogeneous medium. An ideal imaging system is one where all rays originating from a point in the object plane are imaged to one point in the image plane, which is equivalent to creating a spherical wavefront in image space. However, in practice, the equiphase surface for the output light is not a perfect sphere for some or, most often, any of the field points. The deviation from a spherical wavefront is what we refer to as optical aberrations. Freeform optics and metasurfaces are two types of optical devices that enable manipulation of the output wavefronts and thus can be used to build systems with high imaging performance.

Freeform optical surfaces are defined as surfaces with no axis of rotational invariance (within or beyond the optical part) (*16*, *21*–*25*). The removal of the symmetry constraint enables an engineered phase wavefront response due to the different optical path lengths that each ray accumulates by reflecting or refracting from the freeform interface. The path of each ray is dictated by Snell's law that follows directly from Fermat's principle. Systems incorporating freeform surfaces have been shown to achieve diffraction-limited optical performance in compact folded geometries (*12*, *14*, *26*, *27*).

In contrast, metasurfaces achieve wavefront control via light interaction with subwavelength structures that decorate a planar surface. The local phase of the output light is tuned by varying feature properties whose dimensions are on the scale of tens to hundreds of nanometers (for visible wavelength illumination). While the geometric approximation cannot be used to describe the near-field light-matter interaction on a subwavelength scale, the far-field behavior of metasurfaces can be described using Fermat's principle similarly to conventional optics (*28*). The reflection and refraction properties of the flat surface are thus modulated by the subwavelength features based on a generalized Snell's law.

Optical components such as lenses (*29*–*31*) and polarizers (*32*, *33*) have been realized using flat metasurfaces. Subwavelength features of arbitrary shape, designed using inverse optimization, have been used in planar metasurface linear gratings with high diffraction efficiency (*34*). Flat metasurfaces have also been used for optics with more complex phase responses, including holograms (*35*, *36*), cubic lenses, and Alvarez lenses with tunable focal length (*37*). There has also been some effort in non-imaging optics, dealing with cloaking, using metasurfaces to change the reflective properties of micrometer-scale curved interfaces (*38*).

A technique where a flat metasurface fabricated on a flexible substrate is transferred to a cylindrical lens (i.e., a surface with Gaussian curvature of zero) has also been recently demonstrated (*39*). The curved substrate in that work is being masked by the metasurface, similarly to the cloaking application. Although the flexible substrate approach might be adapted to conform a metasurface to a general noncylindrical surface with a nonzero Gaussian curvature, it would require the flexible substrate to be stretched, compressed, or torn [as per Gauss' Theorema Egregium (*40*)]. Guaranteeing that each metasurface feature will be conformed at the correct position on the surface requires a detailed study of the material properties of the flexible metasurface. For the general case of a freeform substrate, this process, if achieved, might be challenging to scale with high reproducibility.

Thus, to the best of our knowledge, there has not been any realization of a generalizable design-to-fabrication process for creating metasurfaces on a freeform substrate where both the metasurface

---

[1]The Institute of Optics, University of Rochester, Rochester, NY 14627, USA. [2]JEOL USA Inc., 11 Dearborn Rd., Peabody, MA 01960, USA. [3]Department of Physics, University of Rochester, Rochester, NY 14627, USA. [4]Center for Coherence and Quantum Optics, University of Rochester, Rochester, NY 14627, USA. [5]Materials Science Program, University of Rochester, Rochester, NY 14627, USA. [6]Center for Freeform Optics, University of Rochester, Rochester, NY 14627, USA. [7]Center for Visual Science, University of Rochester, Rochester, NY 14627, USA.

*Corresponding author. Email: nick.vamivakas@rochester.edu (A.N.V.); rolland@optics.rochester.edu (J.P.R.)

phase response and the shape of the freeform optic are leveraged for imaging and aberration correction. In the current work, we present a design-to-fabrication framework building on the design method for freeform optics developed by Bauer *et al.* (*19*) and an enhanced electron beam lithography (EBL) process for metasurface fabrication on a freeform substrate. We demonstrate the feasibility and advantages of the framework with a design of a near-eye-display–inspired imager.

Metaform working principles

We first propose the concept of a metaform optic (see Fig. 1)—an optical surface with an engineered phase response provided by a metasurface conformed to a freeform substrate. To explain the working principle of the metaform, we shall first assume that spatially and temporally coherent light is incident on the metaform. The light interacts with the freeform surface geometry, accumulating phase from optical path differences and additionally accumulating phase from the light-matter interaction with the nanoscale metasurface features. Let us first consider a freeform surface defined by points in space denoted as $\boldsymbol{r} = [x, y; z(x, y)]$, where $z(x, y)$ is the freeform surface departure from the plane (x, y) from which the surface shape is defined (as shown in Fig. 1A). For simplicity, we will consider the reflection of light from the metaform surface, although the working principles of the device are similarly applied for refraction. Let A be a point on an incident ray and B a point on the corresponding reflected ray as seen in Fig. 1C. The phase delay that light accumulates from reflection off the freeform surface at point $[x_0, y_0; z(x_0, y_0)]$ via propagation is then given by

$$\phi_{\text{freeform}}(x_0, y_0; z(x_0, y_0)) = \phi(\boldsymbol{B}) - \phi(\boldsymbol{A}) = \int_A^B d\phi(\boldsymbol{r}) = \int_A^B \boldsymbol{k} \cdot d\boldsymbol{r} \quad (1)$$

where $\boldsymbol{k}$ is the wave vector. We can then use the general stationary phase version of Fermat's principle to describe the light behavior at the freeform surface interface, leading to the conventional Snell's law of reflection and refraction.

Next, we need to consider the phase contributed by the light interaction with the conformed metasurface. In the ideal case, the abrupt phase shift provided by the metasurface is defined continuously along the freeform surface. However, in practice, the desired metasurface phase is first discretely sampled along the (x, y) plane, similarly to Fig. 1A, with a step size smaller than the wavelength of light. Then, carefully selected optically thin resonators (nano-tokens) are placed at each discrete point, as shown in Fig. 1C, to provide the device's desired phase and amplitude response. As the freeform surface slope varies over a much longer range than the wavelength of light and the nano-tokens are much smaller than the wavelength, we can consider the immediate region around each token to be flat and oriented at some angle. A ray of light intersecting the combined metaform at a point $[x_0, y_0; z(x_0, y_0)]$ then accumulates the propagation phase from Eq. 1 and an additional abrupt phase $\phi_{\text{meta}}(x_0, y_0)$ from the light interaction with the nano-tokens. Thus, we can express the total phase that a ray intersecting the combined metaform at a point $[x_0, y_0; z(x_0, y_0)]$ accumulates as

$$\phi_{\text{metaform}}(x_0, y_0; z(x_0, y_0)) = \phi_{\text{meta}}(x_0, y_0) + \int_A^B \boldsymbol{k} \cdot d\boldsymbol{r} \quad (2)$$

Therefore, for a general point along the metaform, we can write the total phase contribution of the device as

$$\phi_{\text{metaform}}(x, y; z(x, y)) = \phi_{\text{meta}}(x, y) + \phi_{\text{freeform}}(x, y; z(x, y)) \quad (3)$$

By applying Fermat's principle, we can also think of Eq. 3 in terms of angles instead of phase, similarly to the generalized Snell's law as defined by Yu *et al.* (*28*). From a ray perspective, these angles are determined by the path of least time that light chooses to take when reflecting between two points. Equivalently, from a wave perspective, the angles are calculated on the basis of the derivative of the reflected phase profile (i.e., the propagation vector perpendicular to the wavefront). In both cases, the incident light is redirected by an angle equal to the sum of the angular contribution from the freeform optics (based on the conventional law of refraction and reflection) and the additional contribution from the local light interaction with the metasurface.

The simple addition of the phase/angular contributions significantly simplifies the design of a metaform. Furthermore, the capability to distribute the phase response complexity between the freeform optics and the metasurface allows us to leverage the advantages of both technologies. For instance, consider Fig. 1 that shows a scenario where a metaform is used as part of an imaging system. The total device phase ϕ_{metaform} is the desired optical response of the metaform so that it focuses the light and creates an image satisfying a given target optical performance (e.g., diffraction limited). The focusing power and the different optical aberration correction

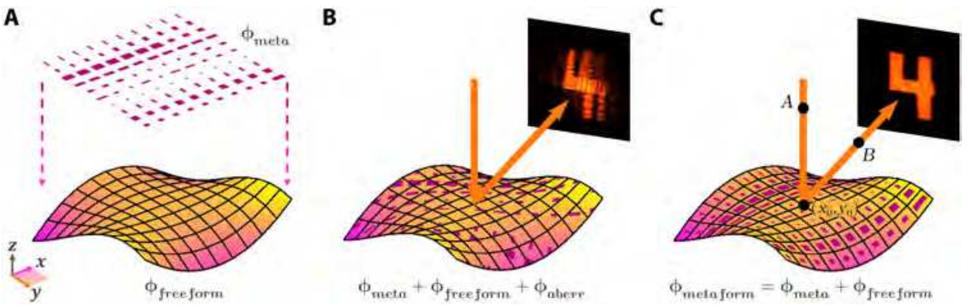

Fig. 1. Conceptual diagram of the formation and function of a metaform. (**A**) The two metaform phase contributions are given by ϕ_{freeform} (the phase imparted by the freeform substrate) and ϕ_{meta} (the phase from the light interaction with the metasurface). (**B**) An example of a metaform where the metasurface is not properly rotated with respect to the freeform substrate, the tokens are not positioned properly along the freeform substrate, and some of the tokens are missing. These inconsistencies result in an additional undesired phase contribution ϕ_{aberr} and associated optical aberrations and blur artifacts in the final image. (**C**) Successful implementation of a metaform where the final phase ϕ_{metaform} imparted to the incoming beam is given precisely by the sum of the as-designed phase contributions from the freeform substrate and the metasurface.

terms can be distributed between the ϕ_{meta} and ϕ_{freeform} terms based on the design, form factor, and fabrication requirements of the system. Thus, the metasurface and the freeform substrate can be co-designed, while their individual phase contributions can be analyzed independently (e.g., using ray-tracing software for the freeform and an electromagnetic field propagation software for the metasurface).

However, although the two components can be designed individually, the spatial relation between the freeform optics and the metasurface features needs to be considered during the full cycle from design to fabrication and testing. In the general case, the freeform optic and metasurface will not have rotational and translational symmetry. Thus, it is essential to define the relative global position and rotation between the two components and keep that relation consistent with the design during fabrication and testing. Similarly, once the local position and orientation of each nano-tokens are chosen in design, the tokens need to be positioned along the freeform surface accordingly during fabrication. If there are global rotational and decenter errors between the metasurface and the freeform substrate, or if the nano-tokens are not correctly distributed along the freeform surface due to fabrication errors or improper conforming of the metasurface, then the total device phase response will not be equal to the as-designed ϕ_{metaform}. Instead, the final device phase contribution will be given by the sum of the two desired contributions from the metasurface and the freeform optic, as well as an additional ϕ_{aberr} term. This additional phase would affect the output wavefront, thus resulting in an aberrated/blurry image, as shown in Fig. 1B. To demonstrate a successful realization of a metaform device, we designed, manufactured, and tested a metaform-based system, as discussed in the next section.

RESULTS

The system of choice is a miniature imager shown in Fig. 2A. The inspiration for the metaform optic is to serve as the combiner for a near-eye display. Near-eye display development is one field where metaforms can be particularly useful for imaging, as the optic that combines the real-world view and the digital image must be conformed to the existing curved glass shape. Furthermore, freeform optics alone cannot necessarily provide the required degrees of freedom, as they are limited by conventional Snell's law. Fresnel reflection can result in optical geometries that have curvature opposite to the natural curvature of the glasses (*41*). A metasurface conformed to the freeform optics can allow a deviation from the Fresnel reflection, thus achieving the desired form factor for combiners where the mechanical tilt of the surface is often not tolerated. For the current proof of concept, the imaging scenario consists of a single metaform mirror that forms a real image of an object located at a finite distance. The system is designed for 632.8-nm visible illumination, and the metaform surface (see Fig. 2B) is formed on a toroidal freeform substrate defined as

$$z_{\text{freeform}}(x,y) = \sqrt{\left(R_y - R_x - \sqrt{R_x^2 - x^2}\right)^2 - y^2} + R_y \tag{4}$$

where R_x and R_y are the two radii of the toroid. The toroidal shape provides a freeform substrate as a pathway to curved combiners in near-eye displays that ergonomically conform to the user's face. This freeform substrate also conveniently provides the power needed to focus the light onto the image plane and is strategically shaped to correct for astigmatism generated by the off-axis geometry. It is essential to realize that we voluntarily did not tilt the substrate to maintain a geometry that is conformal to an aesthetical near-eye display form factor. A tilt of the actual substrate toward the nose, as done in prior art to enable imaging from the temple to the eye (*42*), would result in the notorious "bug-eye" geometry, which is unacceptable to users (*41*). Instead, the off-axis geometry is created by the reflective metasurface design. The metasurface also provides an additional phase contribution to correct residual aberrations

$$\phi_{\text{meta}}(x,y) = \alpha y + \beta x^2 y + \gamma y^3 \tag{5}$$

The full optical specifications of the imager, including the values for R_x, R_y, α, β, and γ, are shown in Table 1.

To understand why the freeform and metasurface are both required for the desired function of the metaform, we can break down the different phase contributions and their role in forming the final image. First, components aligned in the same axes as the object (or the image) cause considerable obscuration and light loss. Freeform optics alone cannot meet that demand, as the Fresnel reflection requires the freeform to be tilted to unobscure the beam, which opposes the form factor specifications for a conformal geometry for near-eye displays. Hence, the metasurface phase is designed to include a linear term that allows unobscured imaging without tilting the actual surface. However, when using an optic in a nonaxial configuration, both rotationally variant and nonvariant aberrations exist that blur the image. The metasurface and the freeform base shape work in tandem to correct the aberrations generated. Specifically,

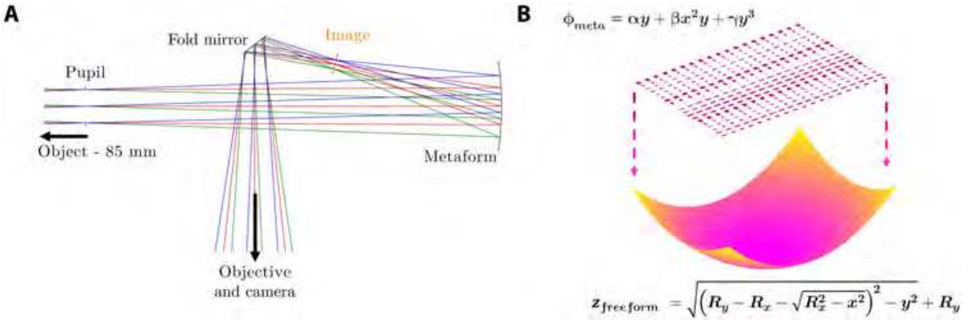

Fig. 2. Miniature imager design using a metaform mirror. (**A**) The object is positioned 85 mm away from the aperture stop. The image is relayed to a CMOS camera using a 51-mm working distance microscope objective (not shown). (**B**) The metasurface is conformed onto the freeform substrate. The metasurface has a predominantly linear phase and some coma contribution for aberration correction. The freeform substrate is an X-toroid as defined in CODE V software and given as Eq. 4.

the freeform base shape was designed as a toroid (instead of a sphere) to first comply with the general shape of eyeglass lenses and in its precise shaping to also correct for the field-constant astigmatism generated by the off-axis geometry; the metasurface was given a coma phase contribution (the second and third term of the phase equation) to mitigate the residual aberrations. Alternatively, we could have added the coma contribution to the freeform substrate. The main decision to integrate coma within the metasurface instead was twofold: (i) to significantly simplify the writing process of the metasurface on an already curved and complexly shaped substrate and (ii) to avoid having to create an even more complexly shaped substrate that would be used in transmission in a see-through architecture (*43*). Thus, the phase contributions for each surface were chosen deliberately, considering the entire design-to-manufacture chain of both the freeform substrate and the metasurface. Critically, the freeform optic and the metasurface synergize within the metaform to create a high-resolution image via a compact, conformal, folded geometry.

Table 1. Optical system specifications for the miniature imager and the metaform.

Parameter	Specification
Object distance	85 mm
Object size	8.5 mm by 5 mm
Illumination wavelength	632.8 nm
Effective focal length	4 mm
F/#	4.67
Magnification	0.0453
Metasurface dimensions	2 mm by 1.5 mm
Freeform substrate shape	X-toroid
R_x, R_y	−8.24 mm, −7.78 mm
α, β, γ	0.2434, −0.0015 mm^{-2}, −0.0017 mm^{-2}

A technical drawing of the designed metaform mirror is shown in Fig. 3A, and the experimentally realized metaform is shown in Fig. 3C. The fabrication challenges demonstrated in Fig. 3B are discussed in Materials and Methods. The full part, 25.4 mm in diameter and made of brass, contains a concave substrate, 6 mm in diameter, at the center of the part. The brass substrate is coated with a 120-nm layer of Ag and a 75-nm layer of SiO_2. These two layers are essential for the function of the used metal-dielectric-metal (Ag-SiO_2-Ag)–type metasurface grating (*44*, *45*). The grating covers the active metaform area of 2 mm by 1.5 mm. The grating subwavelength features are rectangles with varying width and height on the scale of tens to hundreds of nanometers (see Materials and Methods for more information on the selection of tokens). Two sets of four fiducials and a groove for rotation alignment are used for metrology and alignment to achieve the required position and orientation control of the nano-tokens.

Figure 4A shows experimental images of regions from a 1951 United State Air Force (USAF) resolution target imaged using the miniature imager system and the metaform mirror from Fig. 3C. Objects with various dimensions were imaged with spatial frequency features starting from 0.351 line pairs (lp)/mm in the top left corner and increasing to over 5 lp/mm in the bottom right corner. A numerical analysis was used to evaluate the contrast as a function of spatial frequency using the following formula (*46*)

$$\text{Contrast} = \frac{I_{\max} - I_{\min}}{I_{\max} + I_{\min}} \tag{6}$$

where $I_{\max}$ and $I_{\min}$ are the maximum and minimum intensity of a bar in a three-bar target, respectively.

The experimental contrast was evaluated using the images from Fig. 4A for both vertical and horizontal bar targets with varying spatial frequency. The results are shown in Fig. 4B. The $I_{\max}$ and $I_{\min}$ values were evaluated by averaging over a few pixels on the complementary metal-oxide semiconductor (CMOS) camera. The plotted results (blue crosses for the horizontal spatial frequencies and red circles for the vertical spatial frequencies) correspond to the mean

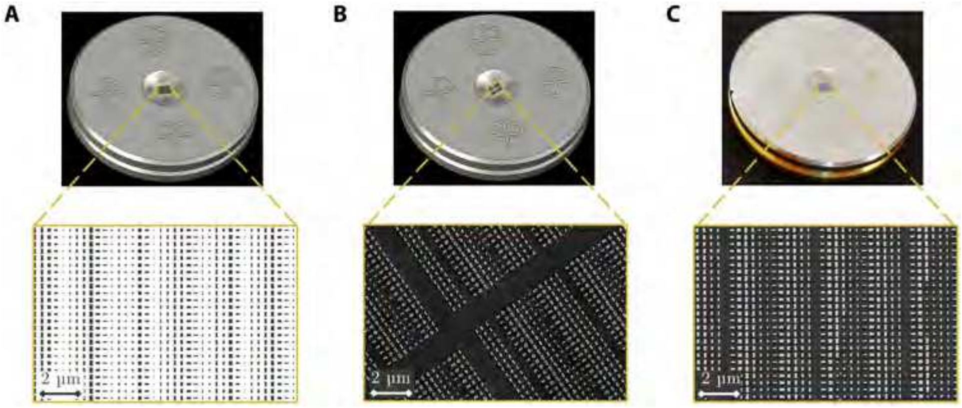

Fig. 3. Design and experimental realization of the metaform mirror for the imager. (**A**) Technical drawing of the part. The dark rectangle in the center corresponds to the area where the metasurface grating is written. The scaled-up inset shows a set of tokens from the metasurface design. (**B**) Example drawing of a metaform with missing tokens and stitching/focusing errors between the different writing zones. An SEM image of a fabricated metaform with these issues is shown at the bottom inset. (**C**) Image of a successful metaform and a scaled-up view of an SEM image of a set of the fabricated nano-tokens. Photo credit: Daniel K. Nikolov, University of Rochester. The three nano-token insets are not necessarily from the same region on the sample, but they are good representatives given the predominantly linear phase nature of the metasurface. The scale on all three insets is 2 μm.

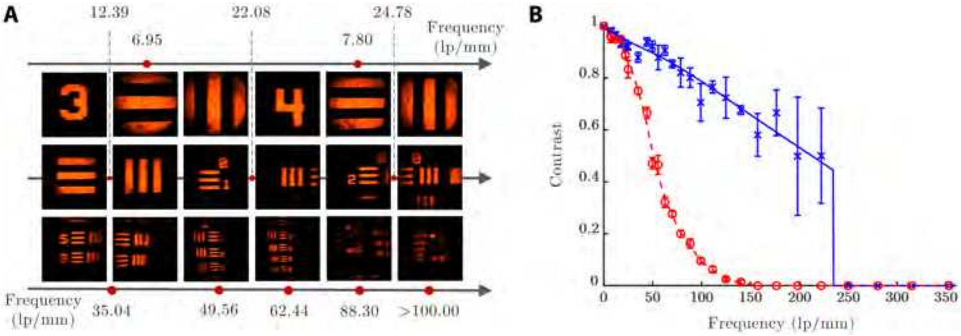

Fig. 4. Experimental imaging results from the metaform. The presented data are collected using the metaform from Fig. 3C. (**A**) Set of different regions of the resolution target imaged via the metaform. The object's spatial frequencies range from 0.315 to >4.53 lp/mm, which corresponds to a range of 6.95 to >100 lp/mm in image space. The features decrease in size from left to right and from top to bottom. (**B**) Measured contrast as a function of spatial frequency (measured in image space). The length of the error bars corresponds to two SDs from the mean. The lines are smooth spline fits to the measured data for the horizontal (blue solid) and vertical (red dashed) frequencies, with fitting weights equal to one over the variance at each point.

intensity, while the error bars represent the SD of the intensity distribution over the chosen pixel region (one error bar is two SDs long). The large error bars for the high horizontal spatial frequencies are due to a low signal-to-noise ratio for the collected data in that regime. A smooth spline fit of the experimental results was also plotted for readability using fitting weights equal to one over the variance at each point.

DISCUSSION

As shown in Fig. 4B, the horizontal features with spatial frequencies in the image plane of <230 lp/mm (<10.42 lp/mm in object space) and the vertical features with spatial frequencies in the image plane of <100 lp/mm (<4.53 lp/mm in object space) were resolved successfully with a contrast of more than 10%. From the experimental results, we can see that the imaging performance of the vertical frequencies is worse than that of the horizontal frequencies. There are a few factors that can explain this finding. A difference between the as-built radii of curvature R_x and R_y and the corresponding as-designed values for the toroid substrate would result in astigmatism and other higher-order aberrations. These discrepancies would be further emphasized by any unevenness in the distribution of the Ag and SiO_2 coating layers that are deposited on the brass substrate. We measured the coated part using an OptiPro UltraSurf noncontact metrology system. The measured sag data were then fitted to a toroid, and the as-built R_x and R_y were calculated to be −8.24 and −7.82 mm, respectively. The derived as-built R_y deviates by ~0.5% from the nominal value, which partially explains the drop in performance for the vertical spatial frequencies. Another possible source of image degradation is residual rotational misalignment errors between the metasurface and the toroid, which are expected to be ±2° based on the alignment procedure detailed in Materials and Methods. The current fabrication process can be further tuned to achieve even higher accuracy of the as-built substrate form and the alignment of the metasurface and the substrate, which would ultimately increase the overall optical performance of the device.

The current device demonstrates a reflective metaform, but the same design and fabrication methods can be extended to realize transmissive metaforms. Furthermore, the proof-of-concept imager that we have presented has dimensions of only 1.5 mm by 2 mm. From a theoretical perspective, there are no limitations to creating metaforms with a footprint of tens of millimeters or even larger, which would be desirable for consumer technology applications. However, some fabrication challenges (like EBL stitching accuracy) may need to be addressed, as discussed in Materials and Methods and the Supplementary Materials.

In the current work, we assumed that the phase and amplitude response of each nano-token does not significantly vary with the angle of incidence variation due to each token's local response. In the imager design that we presented, the freeform surface slope variation is less than ±10° across the clear aperture of 1.5 mm by 2 mm, so this is a reasonable assumption. However, in the general case where the freeform substrate can vary with much higher slopes and the field of view (FOV) may be much higher, the nano-tokens' selection may occur via lookup tables for the phase and amplitude response of tokens with varying height, width, and angle of incidence.

We should also note that most flat metasurfaces in the literature are based on tokens that are equidistant along the device's plane. In the metaform case, this property translates into the tokens being equidistant in the projection plane, as shown in Fig. 1A and discussed in Materials and Methods. However, both the flat metasurfaces and the metaforms may be designed by sampling the phase of the metasurface in a nonuniform way in the x-y plane. We envision that a question of investigation for the metaform case is whether it may be particularly beneficial for the device performance to sample the metasurface with a higher token density in the region of high freeform slopes and/or fast metasurface phase changes. This variable sampling would provide a more continuous phase change across the device and an associated higher device efficiency (*28*, *47*).

The current imager was designed with AR/VR display applications and form factor constraints in mind. However, the imager cannot be integrated into a display design as is. A sketch of an example optical engine for an AR/VR display using a metaform combiner is shown in Fig. 5. The metaform used in the imager above is not see-through. It is inherently opaque due to the Ag backplate required for the function of the metal-dielectric-metal metasurface. This limitation can be overcome by using an array of apertures with random positions and random diameters much larger than the visible wavelength (*43*). The see-through ratio can be adjusted by varying the diameter and density of the apertures. Alternatively, a metaform based on a dielectric metasurface conformed to a transmissive freeform optic can be used. This metaform would be inherently see-through, and a dichroic coating could be applied to adjust

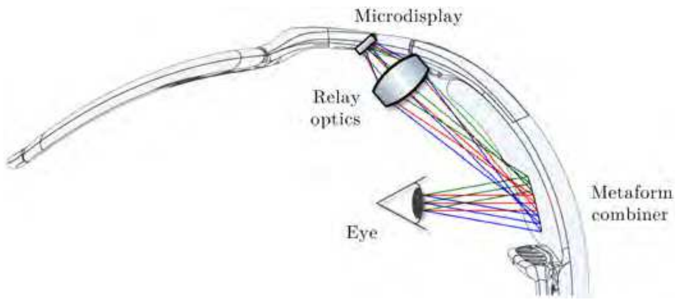

Fig. 5. A top-down view sketch of an example AR eyeglasses architecture. A metaform imager similar to the one presented in this work can be used as an optical combiner.

the brightness ratio between the reflected digital image and the real-world view.

Here, we have introduced the concept and working principles of a metaform—a new type of optical component for imaging applications based on a metasurface conformed to a freeform optical substrate. Each of the two subcomponents' absolute and relative phase must be carefully selected based on the desired device form factor, the aberration theory, and the design framework previously developed by Bauer *et al.* (*19*). The additional degree of freedom enabled by the phase distribution of a metaform allows an optical designer to navigate critical design tradeoffs between optical performance, system volume, and form factor. To demonstrate this new optical component's advantages, we chose the challenging application domain of imagers for AR/VR displays. This type of imager needs to conform within an eyeglass form factor. Thus, it requires the imaging optics to follow the glasses' natural concave curvature without an additional physical tilt. We have demonstrated a miniature imager based on a metaform mirror with a visible design wavelength of 632.8 nm. The resulting system demonstrates successful imaging of features with varying spatial frequencies in object space of up to 10.42 lp/mm. The miniature imager's experimental realization shows the promise of metaform optics to leverage the advantages of metasurfaces and freeform optics for solving challenging optical design problems.

MATERIALS AND METHODS

General design and fabrication consideration

Motivated by the optical design challenges in AR combiners, we endeavored to fabricate a reflective metaform—a metasurface on a reflective freeform substrate. We created an imaging scenario and associated optical design to demonstrate the use of a metaform optic and to provide an apparatus for testing the fabricated device. We chose a metaform with a clear aperture of up to 2 mm in X and Y, which is considered a large writing area for EBL due to the limited size of a single writing zone (typical EBL objective maximum FOV is up to 1 mm by 1 mm). For imaging, an optical system with a 2-mm-diameter part is considered small, so the overall design is expected to be very compact. The actual aperture stop is even smaller (0.8 mm), as it is positioned away from the metaform for aberration corrections, as discussed in the following section. Given the limited amount of flux entering the 0.8-mm aperture stop, setting a small image plane will ensure a sufficient brightness for the image formed on the detector. However, in our reflective off-axis geometry, we also had to balance out potential clearance issues when unobscuring the image. Thus, we set the focal length accordingly to achieve a bright, unobscured image, resulting in a system F/# of about 4.7 for the chosen conjugates and an associated effective focal length of 4 mm. The short focal length and associated image distance hinder the ability to place a sensor at the image for direct detection. Instead, the metaform mirror created an intermediate image that was reimaged to a CMOS sensor using a microscope objective. The reimaging ensured the necessary clearances for the optical components. The details of the design, fabrication, and experimental realization of the imager are described in the following sections.

The small feature size of the metasurface, the rotationally nonsymmetric curved nature of the substrate, and the relatively large metasurface footprint introduced various fabrication challenges. An unsuccessful and the successful realization of the desired metaform surface are shown in Fig. 3, B and C, respectively. The fabrication iterations are further discussed in the Supplementary Materials.

Optical design

When using only reflective optics in an imaging system, attention must be given to the potential obscuration of the light, as it propagates through the system. For optical components aligned along the same axis as the object or image, considerable obscuration occurs, resulting in a loss of light. This challenge can be mitigated by using off-axis sections of surfaces and/or tilted surfaces to ensure that ray clearances are maintained (*48*). However, in cases where a tilted or off-axis surface violates system constraints (like in an AR/VR display), metasurfaces can be leveraged with otherwise centered surfaces to provide the linear phase necessary to redirect the light in the preferred direction. The linear phase is the first metasurface function to be integrated into the metaform.

The second metasurface function of the metaform is aberration correction. As mentioned above, when using an optic in a nonaxial configuration, both rotationally variant and nonvariant aberrations blur the image. The arbitrary phase enabled by a metasurface using higher-order terms than the linear allows correcting the system's aberrations. The aberration correction, however, is split between the freeform optics and the metasurface. The freeform provides astigmatism correction, balancing the aberrations introduced from the linear term of the grating. The metasurface then provides additional coma correction.

The aperture stop location is a critical parameter for the overall aberration correction of the system. The main rotationally variant aberrations generated by the off-axis geometry created via the linear phase term used for unobscuring are field-constant astigmatism, field-constant coma, and field-asymmetric field-linear astigmatism (*19*). If the aperture stop is located at the mirror surface, only the field-constant aberrations can be corrected, leaving a substantial amount of field-dependent astigmatism. By moving the aperture stop in front of the optical surface, however, the field footprints spread out over the surface of the mirror, allowing the additional correction of the field-asymmetric field-linear astigmatism by using a comatic phase term in the metasurface (*49*).

Having the listed considerations in mind, the final imager design is shown in Fig. 2. A third-party optical design software package, CODE V (Synopsys, Mountain View, California, USA) was used for the design's optimization. The complete specifications of the optimized system are listed in Table 1.

Metasurface design

During the imager optical design process, the metasurface was defined in CODE V as an ideal phase polynomial grating. The phase response of this surface was given by an X-Y polynomial, with the polynomial coefficients being varied during optimization. As justified in Introduction, the metasurface component of the metaform can be designed similarly to a flat metasurface as long as the nano-tokens are conformed to the freeform substrate as determined by design. To achieve that specification in the current work, the X-Y polynomial phase from CODE V was sampled discretely over the (x, y) projection in a uniform fashion. This uniform sampling is not required, and in the general case, the distribution of the discrete points can be varied. Once the optimized phase response (given by Eq. 5) was discretized, the metasurface token to be conformed at each discrete point was chosen on the basis of simulations using the finite-difference time-domain (FDTD) software Lumerical (Ansys/Lumerical, Vancouver, BC, Canada).

The simulation process is identical to the one used in previous publications on Ag-SiO_2-Ag metasurface gratings (*44*, *45*). A parameter sweep for a single Ag nano-token with an Ag backplate and a SiO_2 spacer was performed by varying the token width and height (from 40 to 300 nm). The phase and amplitude response of each token was recorded in a lookup table. The phase response of the complete 2 mm by 1.5 mm metasurface was separated into regions of 400 nm by 400 nm that serve as the unit cells of the grating. A token was chosen from the lookup table for each unit cell to match best the design phase at that location while having the highest possible reflectivity (more than 90%). The design was separated into 11 zones with pseudo-equal height (with maximum sag deviation of 10 μm within each zone), and the token information for each zone was saved in a separate layout file for EBL fabrication.

Toroid substrate fabrication

The toroid substrate part was designed to fit in a cassette used for EBL writing on a curved substrate (*50*), as shown in fig. S1. The part is 25.4 mm in diameter and is 4 mm thick. The concave toroid area spanning a 6 mm in diameter circular aperture was fabricated using diamond turning, while the fiducials on the part were laser-etched. Two grooves were first etched on a 1-inch polished brass blank with <10-μm thickness variation. The first was a groove perpendicular to the toroid plane for alignment. The second was a V-groove along the circumference of the blank that was used for mounting the metaform. The blank was centered with respect to its edges on the diamond turning machine where the toroid was fabricated. The part was then moved to the laser etching machine, and the vertical groove was registered to maintain the same rotational alignment as in the diamond turning machine. Two sets of four differentiable fiducials were laser-etched on the part. The first set was on the flat surface of the blank, and the second was inside the concave region. These fiducials were to be used for alignment during the EBL writing, the metrology, and the final imager assembly. The relative rotational error between the fiducials and the toroid axis is ±1°. The corresponding relative decentering error is ±50 μm.

EBL fabrication

The metaform optic was fabricated as follows. The 120-nm-thick Ag (ground layer) and 75-nm-thick SiO_2 were coated on top of the toroid substrate by electron beam evaporation (using PVD 75 Lesker, base vacuum 2×10^{-6} torr, and deposition rate kept at 0.3 Å/s for both Ag and SiO_2). A bilayer electron beam resist containing the 60-nm bottom layer PMMA 495 (A2 in anisole) and the 80-nm top layer PMMA 950 [M2 in methyl isobutyl ketone (MIBK)] were then applied on the substrate by spin coating. The designed metasurface pattern (2 mm by 1.5 mm) was transferred to the bilayer resist by EBL.

EBL on nonplanar substrates is quite challenging due to the inherent limitation of the depth of focus (DOF) of electron beams, which is typically a few tens of micrometers for a 100-kV EBL system. For our nonplanar substrate, the height variation is ~100 μm. We adopted a focal zone splitting technique to write the whole pattern on our toroid substrate (*51*) such that the height deviation in each zone was smaller than the DOF of the EBL objective (to guarantee sharp nano-token features). We divided the whole pattern into zones corresponding to the toroid substrate regions where the height changed by up to 10 μm. These zones had annular-like shapes, and there were 11 zones in total for the 2 mm by 1.5 mm pattern.

The toroid substrate was mounted in the cassette shown in fig. S1B. The edges of two of the outside fiducials (on the flat area of the part) were used to adjust the rotation of the part within the cassette. The circular groove from the diamond turning touch-off was used to locate the apex of the toroid. A Mitaka NH-3N laser probe–based 3D measuring system was then used to find the relative position of the apex of the toroid with respect to markings on the cassette and the fiducials on the brass part. Nickel beads with a diameter of a few tens of nanometers were used to mark one of the fiducials on the flat region of the mirror substrate.

The cassette was then mounted inside a JEOL JBX-6300FS EBL system, as shown in fig. S1A. The nickel bead locations were used to calibrate the EBL coordinate system with the coordinate system of the Mitaka microscope. This procedure guarantees that the JEOL will write the 11 focal zones at the correct X-Y position and height with respect to the apex of the toroid. An objective lens with a maximum square FOV of 62.5 μm by 62.5 μm was used that defines the size of each writing field. The necessary adjustment parameters for the objective lens and the deflector were calculated for each writing field within each focal zone. The parameter values were derived on the basis of a calibration measurement using a slanted Si wafer (*50*). Zones 1 to 11 were then exposed sequentially by adjusting the focusing plane of the objective to be at the mid-height of each zone. The deflector was used to expose the different writing fields within each focal zone.

The part was developed in MIBK:isopropyl alcohol (IPA) (1:3)/IPA (60/30 s) solutions after electron beam writing. An oxygen plasma descum was carried out to remove residual PMMA for 30 s. After that, the Ag nano-tokens were created on the substrate by electron beam evaporation (2-nm chrome was precoated for a good adhesion of Ag on SiO_2), and a lift-off process in Remover PG solution (60°) was applied after the Cr/Ag evaporation.

Metrology

There were multiple steps of metrology measurements done to assure the final metaform quality. Great importance was given to the local and global positions of the metasurface tokens, as discussed earlier. First, the toroid substrate was evaluated after fabrication. The part was visually inspected under an optical microscope. The surface roughness was verified to have a root mean square surface roughness of <3 nm using a Zygo NewView 3D optical surface profiler. The rough toroid orientation with respect to the fiducials was verified using a Zygo Verifire laser interferometer. An accurate surface form measurement was then carried out using an OptiPro UltraSurf noncontact metrology system. The Ag and SiO_2 layers were then deposited, as discussed in the previous section. All the above measurements were then repeated for the coated part. After the metasurface EBL writing, an optical microscope was used to check for centration, rotation, and stitching errors. The final Ag deposition and liftoff were then performed, and the completed metaform part was imaged using a scanning electron microscope (SEM). The actual imaging quality using the metaform was verified in the experimental realization of the imager.

Experimental imager configuration and assembly

A broadband Fianium WhiteLase Micro Supercontinuum laser was used to illuminate the object. A 632.8-nm bandpass filter with 10-nm full width at half maximum was used to match the design wavelength. The laser output was expanded to illuminate the required object size using a 125-mm focal length plano-convex lens and a −25-mm focal length plano-concave lens. A linear polarizer was used to match the illumination polarization in the FDTD metasurface simulations. The object is a USAF 1951 negative, transmissive resolution target. The metaform was mounted via the V-groove inside a lens tube attached to a 5–degree of freedom kinematic stage. A finite conjugate Mitutoyo microscope objective with a 51-mm working distance, numerical aperture of 0.21, and ×10 magnification was used to relay the image to a CMOS machine vision color camera. The exposure settings for the camera were varied to collect two sets of images—a set of saturated images for good visual readability (Fig. 4A) and a set of nonsaturated images for data analysis (used for Fig. 4B). A diagram of the full setup is shown in fig. S2.

SUPPLEMENTARY MATERIALS

Supplementary material for this article is available at http://advances.sciencemag.org/cgi/content/full/7/18/eabe5112/DC1

REFERENCES AND NOTES

1. B. C. Kress, *Optical Architectures for Augmented-, Virtual-, and Mixed-Reality Headsets* (SPIE, 2020).
2. O. Cakmakci, O. A. Martinez, J. Carollo, *Digital Optical Technologies 2019* (International Society for Optics and Photonics, 2019), vol. 11062.
3. H. Huang, H. Hua, High-performance integral-imaging-based light field augmented reality display using freeform optics. *Opt. Express* **26**, 17578–17590 (2018).
4. A. Maimone, A. Georgiou, J. S. Kollin, Holographic near-eye displays for virtual and augmented reality. *ACM Trans. Graph.* **36**, 1–16 (2017).
5. C. Hong, S. Colburn, A. Majumdar, Flat metaform near-eye visor. *Appl. Optics* **56**, 8822–8827 (2017).
6. D. Cheng, Y. Wang, C. Xu, W. Song, G. Jin, Design of an ultra-thin near-eye display with geometrical waveguide and freeform optics. *Opt. Express* **22**, 20705–20719 (2014).
7. A. F. Koenderink, A. Alù, A. Polman, Nanophotonics: Shrinking light-based technology. *Science* **348**, 516–521 (2015).
8. N. A. Rubin, G. D'Aversa, P. Chevalier, Z. Shi, W. T. Chen, F. Capasso, Matrix Fourier optics enables a compact full-Stokes polarization camera. *Science* **365**, eaax1839 (2019).
9. A. Bauer, M. Pesch, J. Muschaweck, F. Leupelt, J. P. Rolland, All-reflective electronic viewfinder enabled by freeform optics. *Opt. Express* **27**, 30597–30605 (2019).
10. A. Arbabi, E. Arbabi, S. M. Kamali, Y. Horie, S. Han, A. Faraon, Miniature optical planar camera based on a wide-angle metasurface doublet corrected for monochromatic aberrations. *Nat. Commun.* **7**, 13682 (2016).
11. M. Khorasaninejad, W. T. Chen, R. C. Devlin, J. Oh, A. Y. Zhu, F. Capasso, Metalenses at visible wavelengths: Diffraction-limited focusing and subwavelength resolution imaging. *Science* **352**, 1190–1194 (2016).
12. E. M. Schiesser, A. Bauer, J. P. Rolland, Effect of freeform surfaces on the volume and performance of unobscured three mirror imagers in comparison with off-axis rotationally symmetric polynomials. *Opt. Express* **27**, 21750–21765 (2019).
13. B. Zhang, G. Jin, J. Zhu, Design method for freeform optical systems containing diffraction gratings. *Opt. Express* **26**, 20792–20801 (2018).
14. J. Reimers, A. Bauer, K. P. Thompson, J. P. Rolland, Freeform spectrometer enabling increased compactness. *Light Sci. Appl.* **6**, e17026 (2017).
15. S.-Q. Li, X. Xu, R. M. Veetil, V. Valuckas, R. Paniagua-Domínguez, A. I. Kuznetsov, Phase-only transmissive spatial light modulator based on tunable dielectric metasurface. *Science* **364**, 1087–1090 (2019).
16. F. Z. Fang, X. D. Zhang, A. Weckenmann, G. X. Zhang, C. Evans, Manufacturing and measurement of freeform optics. *CIRP Ann.* **62**, 823–846 (2013).
17. E. Acosta, J. Sasián, Phase plates for generation of variable amounts of primary spherical aberration. *Opt. Express* **19**, 13171–13178 (2011).
18. N. Yu, F. Capasso, Flat optics with designer metasurfaces. *Nat. Mater.* **13**, 139–150 (2014).
19. A. Bauer, E. M. Schiesser, J. P. Rolland, Starting geometry creation and design method for freeform optics. *Nat. Commun.* **9**, 1756 (2018).
20. M. Born, E. Wolf, *Principles of Optics: 60th Anniversary Edition* (Cambridge Univ. Press, 2019).
21. G. W. Forbes, B. D. Stone, Hamilton's angle characteristic in closed form for generally configured conic and toric interfaces. *J. Opt. Soc. Am. A* **10**, 1270–1278 (1993).
22. O. Cakmakci, B. Moore, H. Foroosh, J. P. Rolland, Optimal local shape description for rotationally non-symmetric optical surface design and analysis. *Opt. Express* **16**, 1583–1589 (2008).
23. G. W. Forbes, Characterizing the shape of freeform optics. *Opt. Express* **20**, 2483–2499 (2012).
24. K. P. Thompson, J. P. Rolland, Freeform optical surfaces: A revolution in imaging optical design. *Optics Photonics News* **23**, 30–35 (2012).
25. J. P. Rolland, M. A. Davies, T. J. Suleski, C. Evans, A. Bauer, J. C. Lambropoulos, K. Falaggis, Freeform optics for imaging. *Optica* **8**, 161–176 (2021).
26. K. Fuerschbach, G. E. Davis, K. P. Thompson, J. P. Rolland, Assembly of a freeform off-axis optical system employing three φ-polynomial Zernike mirrors. *Opt. Lett.* **39**, 2896–2899 (2014).
27. R. Geyl, E. Ruch, R. Bourgois, R. Mercier-Ythier, H. Leplan, F. Riguet, in *International Conference on Space Optics—ICSO 2018* (International Society for Optics and Photonics, 2019), vol. 11180.
28. N. Yu, P. Genevet, M. A. Kats, F. Aieta, J.-P. Tetienne, F. Capasso, Z. Gaburro, Light propagation with phase discontinuities: Generalized laws of reflection and refraction. *Science* **334**, 333–337 (2011).
29. X. Chen, L. Huang, H. Mühlenbernd, G. Li, B. Bai, Q. Tan, G. Jin, C.-W. Qiu, S. Zhang, T. Zentgraf, Dual-polarity plasmonic metalens for visible light. *Nat. Commun.* **3**, 1198 (2012).
30. N. Fang, H. Lee, C. Sun, X. Zhang, Sub-diffraction-limited optical imaging with a silver superlens. *Science* **308**, 534–537 (2005).
31. A. V. Kildishev, A. Boltasseva, V. M. Shalaev, Planar photonics with metasurfaces. *Science* **339**, 1232009 (2013).
32. A. Pors, S. I. Bozhevolnyi, Efficient and broadband quarter-wave plates by gap-plasmon resonators. *Opt. Express* **21**, 2942–2952 (2013).
33. A. Pors, M. G. Nielsen, S. I. Bozhevolnyi, Broadband plasmonic half-wave plates in reflection. *Opt. Lett.* **38**, 513–515 (2013).
34. J. Yang, D. Sell, J. A. Fan, Freeform metagratings based on complex light scattering dynamics for extreme, high efficiency beam steering. *Ann. Phys.* **530**, 1700302 (2018).
35. S. Larouche, Y.-J. Tsai, T. Tyler, N. M. Jokerst, D. R. Smith, Infrared metamaterial phase holograms. *Nat. Mater.* **11**, 450–454 (2012).
36. X. Ni, A. V. Kildishev, V. M. Shalaev, Metasurface holograms for visible light. *Nat. Commun.* **4**, 2807 (2013).
37. A. Zhan, S. Colburn, C. M. Dodson, A. Majumdar, Metasurface freeform nanophotonics. *Sci. Rep.* **7**, 1673 (2017).
38. X. Ni, Z. J. Wong, M. Mrejen, Y. Wang, X. Zhang, An ultrathin invisibility skin cloak for visible light. *Science* **349**, 1310–1314 (2015).
39. S. M. Kamali, A. Arbabi, E. Arbabi, Y. Horie, A. Faraon, Decoupling optical function and geometrical form using conformal flexible dielectric metasurfaces. *Nat. Commun.* **7**, 11618 (2016).
40. C. F. Gauss, *Disquisitiones Generales Circa Superficies Curvas* (Typis Dieterichianis, 1828).
41. B. Kress, T. Starner, A review of head-mounted displays (HMD) technologies and applications for consumer electronics. *Proc. SPIE* **8720**, 87200A (2013).
42. J. P. McGuire Jr., *Emerging Liquid Crystal Technologies V* (International Society for Optics and Photonics, 2010), vol. 7618.
43. D. K. Nikolov, F. Cheng, L. Ding, A. Bauer, A. N. Vamivakas, J. P. Rolland, See-through reflective metasurface diffraction grating. *Opt. Mater. Express* **9**, 4070–4080 (2019).
44. A. L. Kitt, J. P. Rolland, A. N. Vamivakas, Visible metasurfaces and ruled diffraction gratings: A comparison. *Opt. Mater. Express* **5**, 2895–2901 (2015).
45. D. K. Nikolov, F. Cheng, N. Basaran, A. Bauer, J. P. Rolland, A. N. Vamivakas, Long-term efficiency preservation for gradient phase metasurface diffraction gratings in the visible. *Opt. Mater. Express* **8**, 2125–2130 (2018).
46. A. A. Michelson, *Studies in Optics* (Courier Corporation, 1995).

47. J. W. Goodman, *Introduction to Fourier Optics* (Roberts and Company Publishers, 2005).
48. L. G. Cook, Reflective optical triplet having a real entrance pupil, U.S. Patent 4,733,955 (1988).
49. K. Fuerschbach, J. P. Rolland, K. P. Thompson, Theory of aberration fields for general optical systems with freeform surfaces. *Opt. Express* **22**, 26585–26606 (2014).
50. V. Ray, Y. Aida, R. Funakoshi, H. Kato, S. W. Pang, High resolution patterning on nonplanar substrates with large height variation using electron beam lithography. *J. Vacuum Sci. Technol. B* **30**, 06F303 (2012).
51. D. Wilson, P. Maker, R. Muller, P. Mouroulis, J. Backlund, Recent advances in blazed grating fabrication by electron-beam lithography. *Proc. SPIE* **5173**, 51730E (2003).
52. R. Peng, D. Wang, Z. Hu, J. Chen, S. Zhuang, Focal length hysteresis of a double-liquid lens based on electrowetting. *J. Opt.* **15**, 025707 (2013).

Acknowledgments: This work was performed, in part, at the University of Michigan Lurie Nanofabrication Facility. We would like to thank M. Pomerantz and D. Teverovsky for their assistance in using the UltraSurf metrology equipment, L. Qiu for his assistance in the Ag deposition and liftoff for the final metaform, and G. Gandara-Montano for stimulating discussions on measuring optical contrast. This research is synergistic with the National Science Foundation I/UCRC Center for Freeform Optics (IIP-1338877, IIP-1338898, IIP-1822049, and IIP-1822026). **Funding:** This work was supported partially by a fellowship from the Link Foundation and funding from the Center for Emerging and Innovative Sciences. **Author contributions:** D.K.N. co-designed the metasurface and prepared the design for fabrication, created software tools for analyzing the metaform optical performance, guided the freeform substrate fabrication, performed metrology measurements of the freeform mirror, contributed to the EBL alignment, designed and built the experimental imaging setup, collected and analyzed the imaging results, and prepared the manuscript draft (incorporating text from the other authors). A.B. designed the miniature imager including the reimaging arm, developed tools for analyzing the optical performance of the metaform, and contributed to the manuscript text. F.C. co-designed the metasurface, prepared the freeform mirror for EBL, assisted in developing the EBL process, led the EBL fabrication, performed SEM imaging, and contributed to the manuscript text. H.K. assisted and debugged the development of the EBL process and directed the use of the JEOL machine for the EBL fabrication. A.N.V. and J.P.R. conceived and supervised the project. All authors discussed the results and revised the manuscript. **Competing interests:** The authors declare that they have no competing interests. **Data and materials availability:** All data needed to evaluate the conclusions in the paper are present in the paper and/or the Supplementary Materials. Additional data related to this paper may be requested from the authors.

Submitted 26 August 2020
Accepted 11 March 2021
Published 30 April 2021
10.1126/sciadv.abe5112

Citation: D. K. Nikolov, A. Bauer, F. Cheng, H. Kato, A. N. Vamivakas, J. P. Rolland, Metaform optics: Bridging nanophotonics and freeform optics. *Sci. Adv.* **7**, eabe5112 (2021).

Science Advances

Metaform optics: Bridging nanophotonics and freeform optics

Daniel K. Nikolov, Aaron Bauer, Fei Cheng, Hitoshi Kato, A. Nick Vamivakas and Jannick P. Rolland

Sci Adv **7** (18), eabe5112.
DOI: 10.1126/sciadv.abe5112

Science Advances (ISSN 2375-2548) is published by the American Association for the Advancement of Science, 1200 New York Avenue NW, Washington, DC 20005. The title *Science Advances* is a registered trademark of AAAS.